Emergence of topological nodal lines and type-II Weyl nodes in the strong spin-orbit coupling system InNbX_{2} (X=S,Se)

Yongping Du, Xiangyan Bo, Di Wang, Er-jun Kan, Chun-Gang Duan, Sergey Y. Savrasov, and Xiangang Wan

Phys. Rev. B **96**, 235152 — Published 29 December 2017

DOI: 10.1103/PhysRevB.96.235152

Emergence of Topological Nodal Lines and Type II Weyl Nodes in Strong Spin–Orbit Coupling System $InNbX_2$(X=S,Se)

Yongping Du,[1] Xiangyan Bo,[2] Di Wang,[2] Er-jun Kan,[1] Chun-Gang Duan,[3,4] Sergey Y. Savrasov,[5,*] and Xiangang Wan[2,6,†]

[1]*Department of Applied Physics, Nanjing University of Science and Technology, Nanjing, Jiangsu 210094, China*
[2]*National Laboratory of Solid State Microstructures and Department of Physics, Nanjing University, Nanjing 210093, China*
[3]*Key Laboratory of Polar Materials and Devices, Ministry of Education, East China Normal University, Shanghai, 200241, China*
[4]*Collaborative Innovation Center of Extreme Optics, Shanxi University, Taiyuan, Shanxi 030006, China*
[5]*Department of Physics, University of California, Davis, One Shields Avenue, Davis, California 95616, USA*
[6]*Collaborative Innovation Center of Advanced Microstructures, Nanjing University, Nanjing 210093, China*

(Dated: November 20, 2017)

Using first–principles density functional calculations, we systematically investigate electronic structures and topological properties of layered materials $InNbX_2$ (X=S, Se). In the absence of spin–orbit coupling (SOC), both compounds show nodal lines protected by mirror symmetry. Including SOC, the Dirac rings in $InNbS_2$ split into two Weyl rings. This unique property is distinguished from other discovered nodal line materials which normally require the absence of SOC. On the other hand, SOC breaks the nodal lines in $InNbSe_2$ and the compound becomes a type II Weyl semimetal with 12 Weyl points in the Brillouin Zone. Using a supercell slab calculation we study the dispersion of Fermi arcs surface states in $InNbSe_2$, we also utilize a coherent potential approximation to probe their tolerance to the surface disorder effects. The quasi two–dimensionality and the absence of toxic elements makes these two compounds an ideal experimental platform for investigating novel properties of topological semimetals.

PACS numbers: 71.20.-b, 73.20.-r, 71.20.Lp

I. INTRODUCTION

In the past few years, topological semimetals, such as Weyl semimetals (WSM) [1, 2], Dirac semimetals (DSM) [3–9] and Nodal Line semimetals (NLS)[10–13], have received tremendous research interest. In a Weyl semimetal, the electrons around Weyl points, which are the crossing points of two non–degenerate linearly dispersing energy bands, behave exactly like Weyl fermions[1, 2]. With definite chirality, each Weyl point can be considered as a topologically protected charge, thus extending classification of topological phases of matter beyond insulators[1, 2]. Weyl points are extremely robust against weak perturbations and can only be annihilated when pairs of Weyl points with opposite topological charge meet with each other. Then the system opens a gap evolving into either a normal insulator or an Axion insulator[1, 14].

One of the most remarkable properties of WSMs is the existence of topological surface states in a form of Fermi arcs[1]. This serves as an unambiguous evidence to identify this state of matter. A great number of other exotic phenomena has also been proposed for WSMs: a highly anisotropic negative magnetoresistance related to chiral anomaly effect[15, 16], a topological response[17], unusual non–local transport properties[18], novel quantum oscillations from Fermi arcs[19], etc.

A further classification here has been given to distinguish WSMs whose bulk Fermi surfaces shrink to Weyl points (called type I), or to exotic hyperboloid surfaces (called type II), where the cones are titled and induce a finite density of states at the nodal point[20]. Due to the tilted nature of the nodes, the low energy excitations break Lorentz invariance, cause absence of the chiral anomaly at certain magnetic–field angles, magnetic breakdown and novel Klein tunneling [20, 21].

There has been a great progress in searching for signatures of WSMs in real materials. Starting from the original proposal on pyrochlore iridates [1], several systems, such, e.g., as $HgCr_2Se_4$ [22], TaAs[23, 24], WTe_2[20], NbP[25], TaP[26], NbAs[27], $MoTe_2$[28], MoP_2, WP_2[29], LaAlGe[30], etc. have been predicted to exhibit WSM behavior. A large amount of recent experimental work has been devoted to study properties of TaAs family [25–27, 31–34]. In many of the proposed materials, however, the Weyl points do not exactly cross but only close to the Fermi level, and also there are trivial Fermi states. The contribution from these trivial states significantly complicates the analysis of topological surface states and their novel transport behavior.

In addition to WSMs, a three–dimensional (3D) DSM [3–9] has also been proposed. The Dirac points in DSM are four–fold degenerate, and can be viewed as a merge of two Weyl fermions with opposite chirality in the Brillouin zone (BZ). The Dirac points usually require a protection by time reversal, inversion and additional crystal

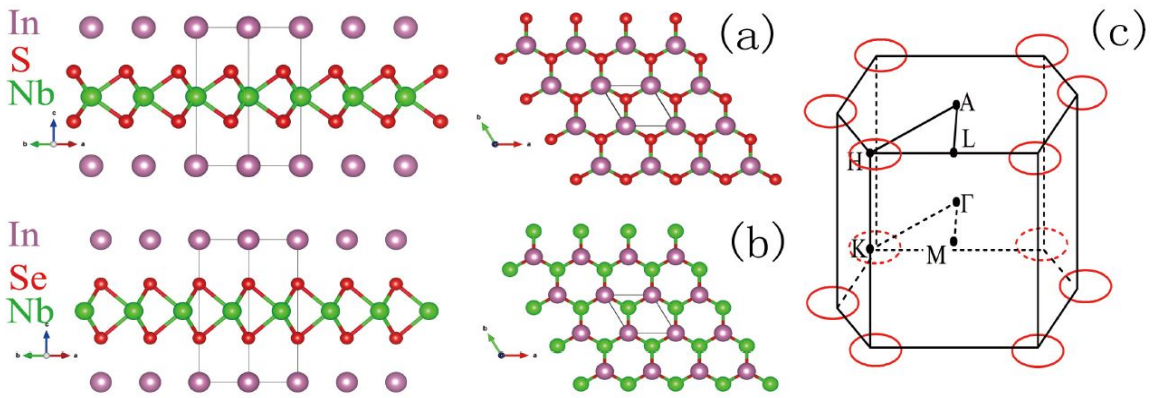

FIG. 1: (color online). (a) Side view (left) and top view (right) of crystal structure of $InNbS_2$; (b) Side view (left) and top view (right) of crystal structure of $InNbSe_2$. Green, violet, and red spheres represent Nb, In, and S (Se) atoms, respectively. (c)The schematic of the nodal lines in $InNbX_2$ (X=S,Se).

symmetry [4–7].

Different from WSMs and DSMs which have finite numbers of band touching points in the BZ, a third topological semimetal, NLS has a whole crossing line in momentum space[10–13]. Same as 3D DSM, NLS also needs crystal symmetry to stabilize its band crossing line [5, 35]. The most exotic property of NLS is its two dimensional (2D) drumhead–like surface state[10–13, 36–44]. It has been speculated that this special state may realize high–temperature superconductivity [45, 46].

Several materials have been predicted to be topological NLSs [10–13, 36–44]. However, most of these predictions are based on calculations without spin–orbit coupling (SOC) [11–13, 36–42], inclusion of which leads normally to gapping out the nodal line [11–13, 36–42]. Only in a few systems, this was found to be not the case, where $TlTaSe_2$ and $PbTaSe_2$ are predicted to remain NLS behavior in calculations with SOC [43, 44].

Compared with 3D systems, quasi–2D layered materials are easier to cleave and study their surface electronic structures, and more favorable from the experimental perspective. Also, toxic elements like As, P, Tl and Hg found in many of the discovered materials create additional complications. Thus, searching for new topological systems and finding ways to remove the effects of trivial states meanwhile preserving contributions from topological Fermi arcs, are important problems of this emergent field of condensed matter physics.

In this work, we use first–principles calculations based on density functional theory (DFT) in its generalized gradient approximation (GGA) [47] to predict that $InNbS_2$ and $InNbSe_2$ show nodal lines and Weyl semimetal behavior, respectively. Without considering SOC, both of them are NLSs, and the band crossing lines are formed by four–fold degenerate Dirac points. The nodal lines, which are located around H point in the $k_z = \pi$ plane (i.e. L-H-A plane) in the BZ, are protected by the mirror symmetry. Including SOC, the four–fold degenerate nodal line in $InNbS_2$ splits into two Weyl type nodal lines which are again protected by the mirror symmetry. On the other hand, the SOC changes $InNbSe_2$ to a type II WSM for which we predict the Fermi arc surface states to appear on a easily cleavable (001) Indium terminated surface. Using a combination of DFT with Coherent Potential Approximation (CPA) we also simulate the effects of surface disorder to study the robustness of the Fermi arcs in this system. Our theoretical work shows that $InNbS_2$ and $InNbSe_2$ are very promising materials for studying NLSs and WSMs, respectively.

II. CRYSTAL STRUCTURE

$InNbX_2$ (X=S, Se) have already been synthesized experimentally and the crystal structures of them belong to space group $P\bar{6}m2$ (NO. 187) which is non–centrosymmetric[48–50]. The In layer is intercalated between two niobium dichalcogenides layers. As shown in Fig. 1(a) and Fig. 1(b), the mirror plane is located at In layer or Nb layer. As discussed later in our work, this mirror plane plays a key role in protecting the nodal line. As shown in Fig.1, the In atoms in $InNbS_2$ are aligned with Nb atoms in the vertical direction, while in $InNbSe_2$, they are aligned with Se atoms. This difference in the lattice structure results in different topological features for these two compounds. We also fully relax the lattice constants and the coordinates of atoms included van der Waals interaction[51]. The numerical results are in good agreements with experiments[52], and the small discrepancy between the numerical and experimental structures has negligible effect on the electronic property. Hence, the following results are obtained based on the experi-

mental structure, unless stated specifically.

III. RESULTS FOR $InNbS_2$

Here we discuss our band structure results for $InNbS_2$. We perform its density functional GGA calculation by using a full potential linear muffin tin orbital (FP–LMTO) method [53] and also cross check the results with linearized augmented plane wave method as implemented in WIEN2K package [54]. Both methods provide identical electronic structures. The orbital character analysis shows that $3s$ and $3p$ bands of S atoms are mainly located at -14 to -12 eV and -7 to -1 eV, respectively. This indicates that the S–$3s$ and S–$3p$ orbits are almost completely filled. Nd–$5d$ states, which are mainly located between -1 and 4 eV, have also a spectral weight between -7 and -1 eV, indicating a considerable hybridization between Nb and S. On the other hand, In–$5p$ bands are distributed mainly above -1 eV. As shown in Fig.2(a), the bands around the Fermi level are mainly contributed by Nb–$5d_{x^2-y^2}/5d_{xy}$ and In–$6p_x/6p_y$ states. The Nb–$5d_{x^2-y^2}/5d_{xy}$ bands are higher in energy than the In–$6p_x/6p_y$ states, however, there is a band inversion around H point as shown in Fig. 2(c). This band inversion has also been confirmed by the modified Becke-Johnson (mBJ) exchange potential calculations [55]. Since L–H–A plane possess mirror symmetry, the In–$6p_x/6p_y$ (Nb–$5d_{x^2-y^2}/5d_{xy}$) states around H point can be classified in terms of the mirror eigenvalues -1 $(+1)$, as shown in Fig. 2(c). Combining with the time reversal symmetry, this band inversion guarantees a nodal line in the L–H–A plane [43, 44]. The schematics of the nodal lines in $InNbS_2$ is shown in Fig. 1(c).

To clarify the origin of the band inversion at H point, we calculate the electronic structure of $InNbS_2$ by applying an in–plane tensile strain. We denote the magnitude of the in–plane strain by $(a - a_0)/a_0$, where a and a_0 denote lattice parameters of the strained and unstrained systems, respectively. Our calculation reveals that the energy difference between In–$6p_x/6p_y$ state and Nb–$5d_{x^2-y^2}/5d_{xy}$ states decreases as the in–plane tensile strain increases, and when the in–plane strain becomes larger than 7%, the band inversion at H point disappears. Therefore, the band inversion originates from the crystal field effect instead of SOC.

To explore the role of the mirror symmetry, we break it by shifting a Nb atom by $0.01\mathring{A}$ along z direction. Without mirror symmetry, the In–$6p_x/6p_y$ and Nb–$5d_{x^2-y^2}/5d_{xy}$ states belong to the same irreducible representation and can hybridize with each other. Thus, the band crossing around the H point becomes gapped as shown in Fig. 2(e). This clearly demonstrates that the nodal line in $InNbS_2$ is indeed protected by the mirror symmetry.

As a relativistic effect, SOC always exists. Thus we also perform the calculation to check the effect of SOC. Without inversion, SOC splits each band into two branches as shown in Fig. 2(b). As a result, there are spinfull bands near the Fermi level as shown in Fig.2(d). Due to the mirror symmetry at L–H–A plane, we can classify these four bands by mirror eigenvalues $\pm i$. Two red bands have mirror eigenvalues $-i$, while blue ones have mirror eigenvalues i. As a result, the order of mirror eigenvalues of four bands are $(+i, -i, +i, -i)$ (sorting from high energy to low energy at H point, labeled as band 1, 2, 3, 4), shown in Fig. 2(d). Since SOC does not eliminate the band inversion, two band with different mirror eigenvalues form two separate Weyl rings around the H point. Furthermore, nodal line can be characterized by the Berry phase[10–13, 36–44], our numerical results show that the Berry phase of these two separate Weyl rings are the same, i.e. π. These unique two separated nodal lines can have unique surface state as discussed in Refs. [42–44]. When mirror symmetry is broken, four bands around H point are found to belong to the same irreducible representation. Consequently the Weyl rings are gapped out as shown in Fig. 2(f). This again shows that the mirror symmetry play a key role in protecting the nodal lines in $InNbS_2$.

IV. RESULTS FOR $InNbSe_2$

We now discuss our band structure calculation for $InNbSe_2$. The results without and with SOC are shown in Figs. 3(a) and (b), respectively. Our orbital–character analysis reveals that the states near the Fermi level are mainly contributed by Nb–$5d_{x^2-y^2}/5d_{xy}$ (denoted by red color) and In–$6p_x/6p_y$ (denoted by blue color). However, both GGA and mBJ calculations predict that the energy of Nb–$5d_{x^2-y^2}/5d_{xy}$ is higher than In–$6p_x/6p_y$ at the H point. As a result, there is also a band inversion around the H point, like the case of $InNbS_2$. This is shown in Fig. 3(a). Again, based on the mirror symmetry, the bands around the H point can be classified by their mirror eigenvalues. As shown in Fig. 3(c), the band with a mirror eigenvalue -1 (+1) is marked by blue (red). Thus, similar with $InNbS_2$, time reversal symmetry and the band inversion result in a nodal line around the H point at the mirror plane.

When SOC is included in the calculation, two crossing bands around the H point split into four bands as shown in Fig. 3(b). The detailed band structure around the H point marked in Fig. 3(b) is shown in Fig. 3(d). Different from the situation in $InNbS_2$, the order of the mirror eigenvalues at H point of four bands near the Fermi energy are (+i, -i, -i, +i) (sorting from high energy to low energy, and labeled as band 1, 2, 3, 4). Thus, two bands with the same eigenvalues (i.e. band 2 and 3 with eigenvalues -i) are hybridized and open a gap, other than Weyl rings. However, the further analysis showing that, there

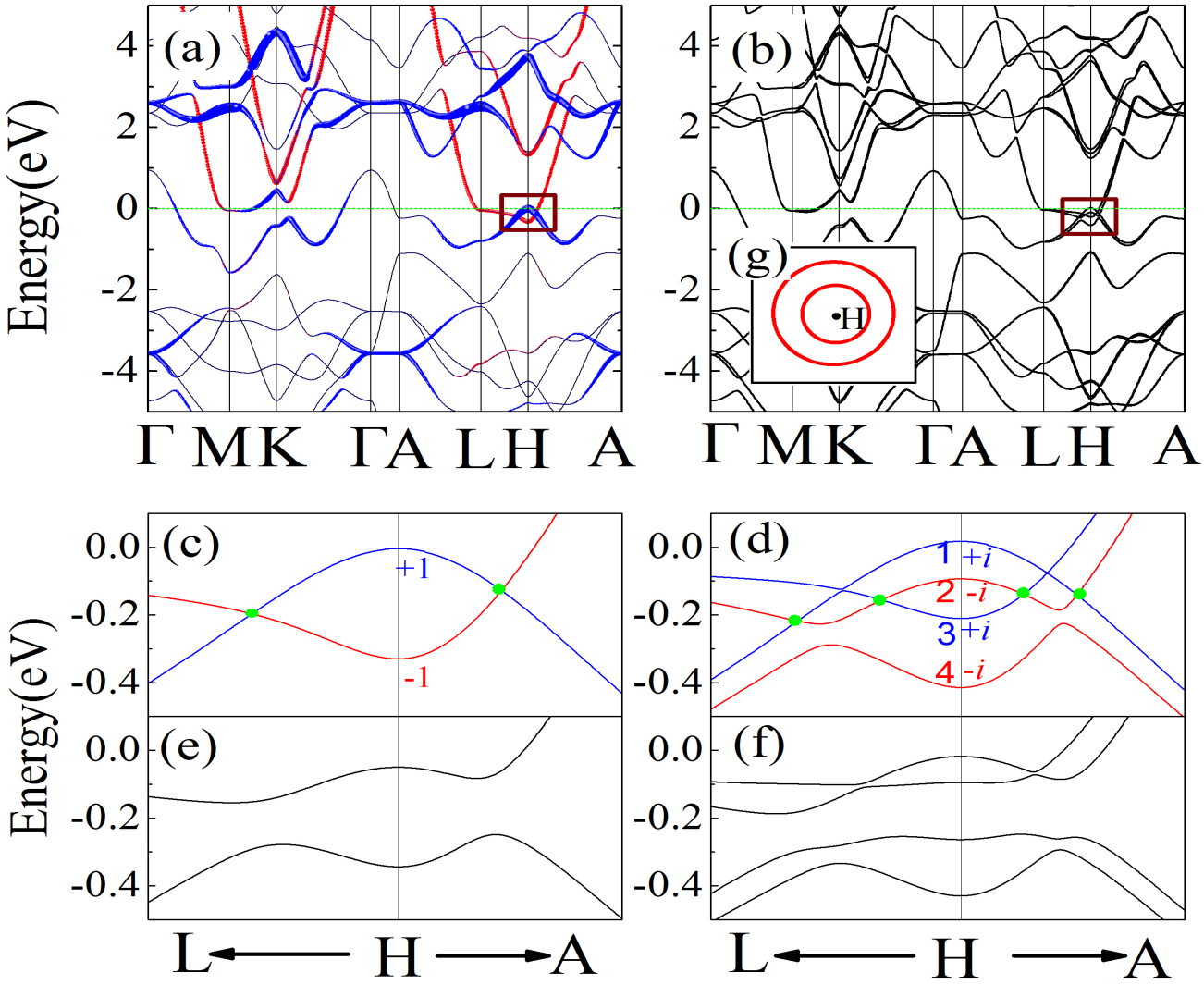

FIG. 2: (color online). (a) Calculated bulk band structure of $InNbS_2$ without SOC. The weights of In-6p_x/6p_y (Nb-5$d_{x^2-y^2}$/5d_{xy}) states are proportional to the width of red (blue) curves. (b) Bulk band structure of $InNbS_2$ calculated with the inclusion of SOC.(c) Closeup of band structure around H point as marked in panel (a). The red line denote the In-6p_x/6p_y states which belong to irreducible representation Γ_2 of space group, while the blue one is the state of Nb-5$d_{x^2-y^2}$/5d_{xy} belonging to irreducible representation Γ_1 of space group. The band with red color has mirror eigenvalue -1, while the blue one has mirror eigenvalue +1. (d) Closeup of band structure around H point near the Fermi energy as marked in panel (b). The red color denotes the mirror eigenvalue $-i$ while the green one denotes the mirror eigenvalue i. (e) and (f) are the band structures around H point with the mirror symmetry broken by shifting Nb atom slightly away from the equilibrium position. (e) without SOC and (f) with SOC. (g) The schematic of the nodal lines around H point in $InNbS_2$ when including SOC.

are band crossing points between band 1 and 2, band 3 and 4, respectively. The mirror eigenvalues between them are different, thus band crossing between them forming two Weyl rings protected by mirror symmetry at L-H-A plane. The different order of mirror eigenvalues and band structure between $InNbS_2$ and $InNbSe_2$ is caused by the different position of In atoms. To further confirm this, We calculate the electronic structure of $InNbSe_2$ in the structure of $InNbS_2$, and vice visa. Our calculations show that, when $InNbSe_2$ is in the structure of $InNbS_2$, it become a node-line semimetal with two separate Weyl rings around H point exactly like the case in $InNbS_2$. And when $InNbS_2$ is in the same structure of $InNbSe_2$, the bands are hybridized and open a gap instead of forming two crossing lines. Interestingly, our further calculation shows that $InNbSe_2$ becomes a Weyl semimetal with 12 Weyl nodes in the first BZ, as shown in Fig. 3(e) and (f). These 12 Weyl points are related

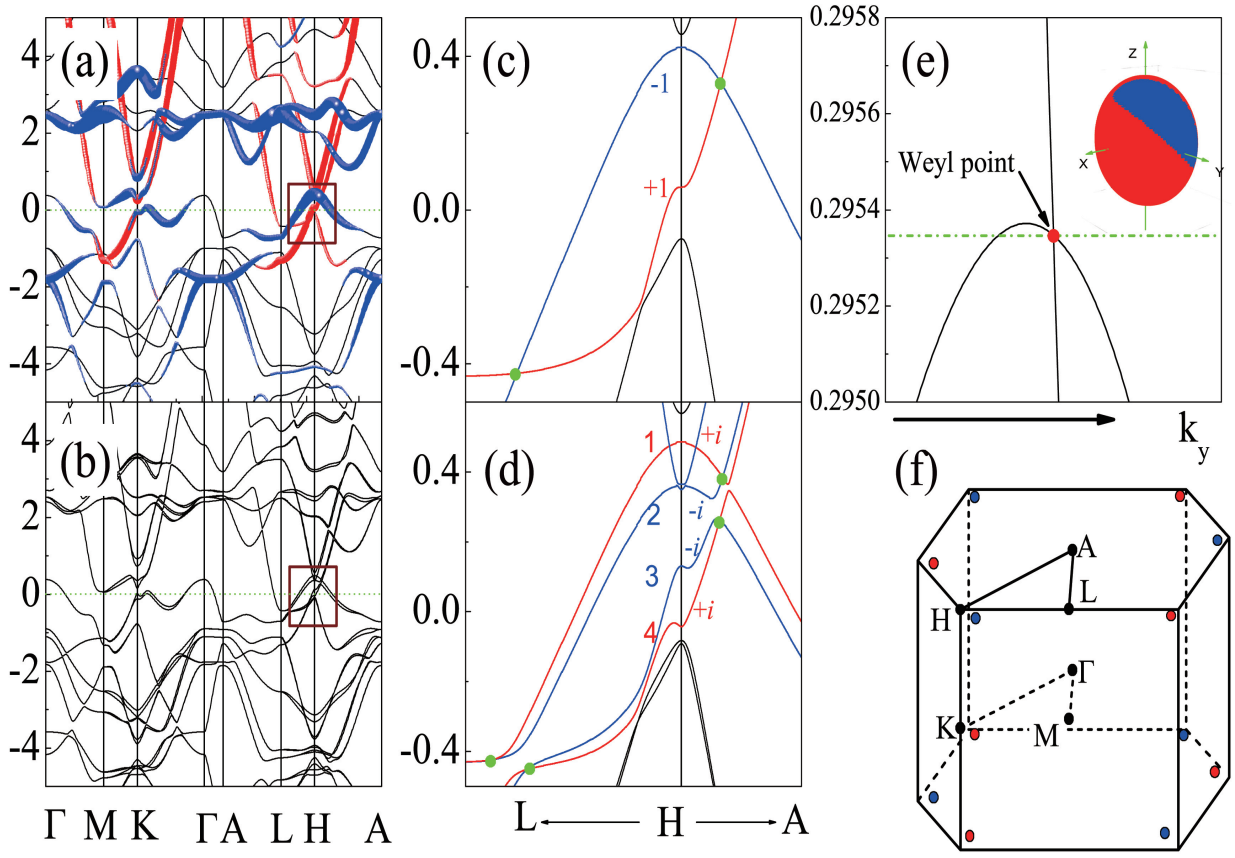

FIG. 3: (color online). (a) Bulk band structure of $InNbSe_2$ without SOC. The weights of In-6p$_x$/6p$_y$ (Nb-5d$_{x^2-y^2}$/5d$_{xy}$) states are proportional to the width of red (blue) curves. (b) Bulk band structure of $InNbSe_2$ including SOC. (c) Closeup of band structure around H point as marked in panel (a). The red denote mirror eigenvalue +1, while the blue denote mirror eigenvalue -1. (d) Closeup of band structure around H point as marked in panel (b). The red denote mirror eigenvalue $+i$, and the blue denote mirror eigenvalue $-i$. (e) band structure around Weyl point. The direction is parallel k_y axis and crossing the Weyl point. The insert is the value of $|T(k)|/|U(k)|$, the magnetic field within the blue area (i.e. $|T(k)|/|U(k)| > 1$) can induce negative magnetoresistence, while the red one ($|T(k)|/|U(k)| < 1$) cannot have negative magnetoresistence[20]. (f) The schematic of the Weyl points in the first Brillouin Zone. Blue (red) color denote the Chern number $+1(-1)$.

with each other by crystal symmetry, consequently they have the same energy. The Weyl points are searched for by scanning the whole BZ.

To confirm the existence of the Weyl points in $InNbSe_2$, we perform Berry curvature integration based on a computational scheme proposed by Fukui *et al*[56]. We define a small cubic region surrounding each Weyl point. A quantity $\gamma^n_{P_l,s}$, which is often called the field strength, is defined as[56, 57]:

$$\gamma^n_{P_l,s} = Im\log(\langle n(\mathbf{k}_l,s)|n(\mathbf{k}_l{+}\mathbf{u}_1,s)\rangle\langle n(\mathbf{k}_l{+}\mathbf{u}_1,s)|n(\mathbf{k}_l{+}\mathbf{u}_1{+}\mathbf{u}_2,s)\rangle\langle n(\mathbf{k}_l{+}\mathbf{u}_1{+}\mathbf{u}_2,s)|n(\mathbf{k}_l{+}\mathbf{u}_2,s)\rangle\langle n(\mathbf{k}_l{+}\mathbf{u}_2,s)|n(\mathbf{k}_l,s)\rangle)$$

where $\mathbf{k}_l$ is a vector at lth mesh point, s=1–6 denotes each of six faces of the cube, $\mathbf{u}_1$ and $\mathbf{u}_2$ are vectors between nearest mesh points for the two directions of the $\mathbf{k}$ vector on the surface of the cube, P_l is lth smallest closed path passing by the points $\mathbf{k}_l$ and its nearest mesh point. In this formula, the Chern number is given by the

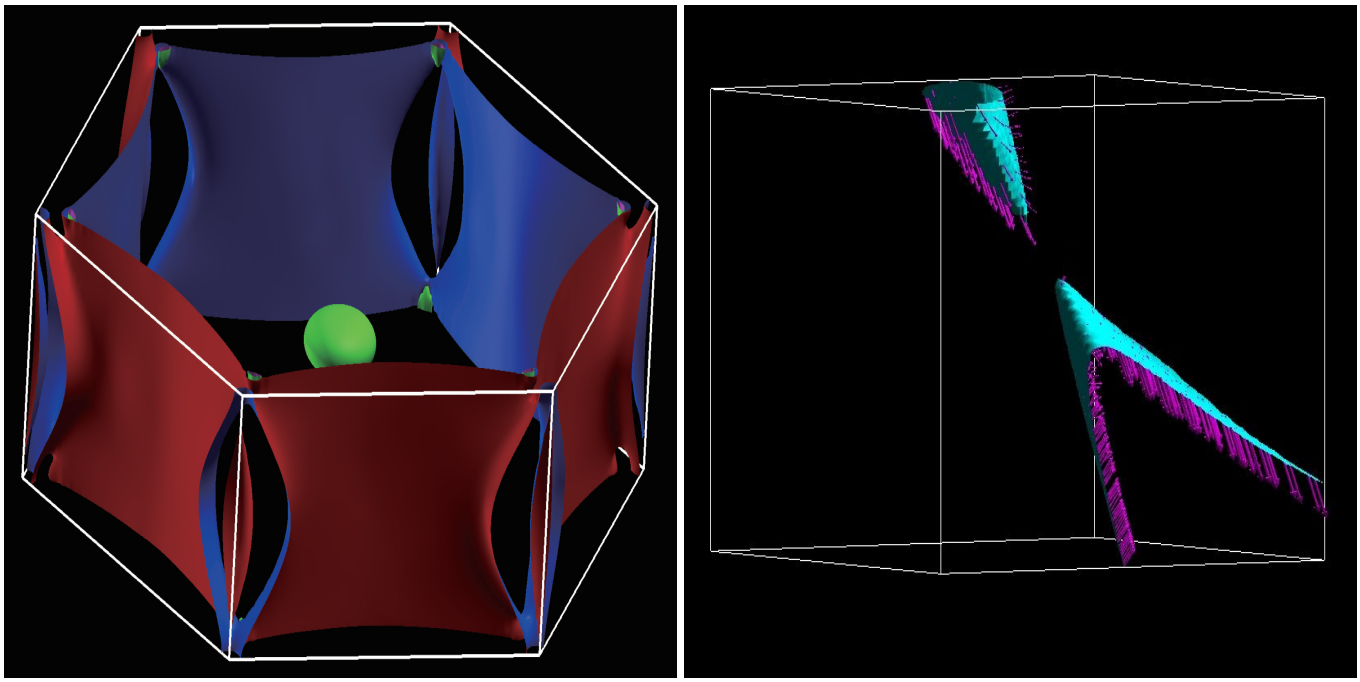

FIG. 4: (color online). Calculated constant energy surface with a slightly shifted position (by 0.2 eV up) of the Fermi level for stoichiometric $InNbSe_2$ showing type II character of the predicted Weyl semimetal: (a) the green–magenta surface is the hole pocket while the red–blue one is the electron pocket. (b) The same but in the immediate vicinity of the Weyl point. Arrows show spin directions of the one–electron states.

sum over coarse mesh of phases $\gamma^n_{P_l,s}$: $C_n = \sum_{P_l,s} \gamma^n_{P_l,s}$. The Bloch wave functions $|n(\mathbf{k}_l, s)\rangle$ are obtained from our first–principles calculations. We employ the 15×15 k-mesh on each of the six faces of the cube, which we found to be sufficient for numerical convergence. We calculate the Chern number of the Weyl point located at (0.298, 0.298, 0.444) using this method and obtain the numerical result equal to +1. The location of this and other Weyl points is schematically shown in Fig. 3(f).

We notice that the Weyl points here exist at the boundaries between electron and hole pockets, therefore the compound can be classified as a type II WSM. Our Fig. 3(e) showing a detailed band dispersion in the vicinity of one Weyl point is very similar to the case of WTe_2[20] where this new type of Weyl points has been recently introduced. They appear due to the tilting term in the linear Weyl Hamiltonian which has led to a finer classification of topological semimetals[20]. Around the Weyl points, the energy spectrum can been written as: $\varepsilon_{\pm}(k) = T(k) \pm U(k)$. As a result, we expect that $InNbSe_2$ will display negative magnetoresistence related to chiral anomaly only when the direction of the magnetic field falls within the cone where $|T(k)|/|U(k)| > 1$ [20] (i.e. the blue area in Fig. 3(e)). We monitor the contact between electron and hole pockets in $InNbSe_2$ by computing the constant energy surface with a slightly shifted position (by 0.2 eV up) of the Fermi level for stoichiometric compound. The result is shown in Fig. 4(a) where the green–magenta surface is the hole pocket while the red–blue one is the electron pocket. We can see that the hole pocket almost touches the electron pocket near the position of the Weyl point. Fig.4(b) shows the same in the immediate vicinity of the Weyl point together with the spin distribution of electronic states shown by arrows. For an ideal Weyl Hamiltonian, the spins are either parallel or antiparallel to the velocities corresponding to the positive/negative chiralities. In real compounds such as $InNbSe_2$, considered here, this becomes only approximate, and as seen in Fig. 4(b), spins show a rather high degree of anisotropy.

V. FERMI ARCS AND EFFECT OF SURFACE DISORDER

In order to examine the Fermi arc surface states of $InNbSe_2$ we determine the one–electron energy bands of 6 unit–cell (24 atomic layers) slab structure using the full potential linear muffin–tin orbital (FP–LMTO) method[53]. The slab is extended along (001) direction and terminated by Se atomic layer at the top and by In atomic layer at the bottom. The spacing between the slabs is set to 12Å. The distance between In and Se atoms is largest in the original unit cell which together with the quasi–two–dimensionality of the crystal structure prompts that this should be most easily cleavable

surface in an experimental setup.

In order to compute the surface Fermi states, we compute surface projected imaginary Green functions

$$ImG(\mathbf{k}, E) = Im \sum_j \frac{\langle \mathbf{k}_j | \hat{P}_s | \mathbf{k}_j \rangle}{E - E_{\mathbf{k}_j} - i\delta}$$

where we set $\delta = 0.001Ry$, and where the surface projector operator $\hat{P}_s$ is chosen as a sum over 4 top/bottom atomic layers τ

$$\hat{P}_s = \sum_{lm\tau} |\phi_{lmt}\rangle\langle\phi_{lm\tau}|.$$

Here $\phi_{lm\tau}$ are the solutions of the radial Schrodinger equation inside a muffin–tin sphere of atom τ taken with the spherically symmetric part of the potential[58].

Fig. 5 shows the result of our calculation, where we visualize $ImG(\mathbf{k}, E)$ as a function of $\mathbf{k}$ by a color (white is 0 and black is $1/\delta = 1000$) within a part of the planar BZ corresponding to the (001) surface unit cell. We distinguish cases for Se terminated (plots a,b) and In terminated (plots c,d) surfaces. Since the Weyl points are located not exactly at the Fermi level, we plot $ImG(\mathbf{k}, E)$ for the energy $E = E_F$, (plots a, c) as well as for the energy $E = E_F + 0.2eV$ (plots b, d) which corresponds to the location of the Weyl points. We note that although (001) surface should be easy to cleave, the chosen atomic configuration assumes that the Weyl points of opposite chiralities project onto the same $\mathbf{k}$–point in the surface BZ. It means that the Fermi arcs extending between opposite chiral charges can potentially start and end at the same projected Weyl point. We found this to be the case for the Se terminated surface where small arcs are clearly visible especially on Fig.5(b) corresponding to the position of the Fermi level tuned to the Weyl point. The situation is more complicated for the In terminated surface where there are essentially two lines that are resolved as connecting the Weyl points on Fig.5(d). We interpret one line to be potentially the Fermi arc and another one to be either a regular surface state or a bulk Fermi state projected to the surface BZ.

In a recent work [59] we argued, based on a simulation of a tight–binding model, that the Fermi arcs should be more surface disorder tolerant than the regular surface states especially in the vicinity of the Weyl points where the arcs electronic wave functions are extended well into the bulk and become less sensitive to the surface disorder. We also found that the particular sensitivity to the surface disorder depends on the shape of the Fermi arc with the straight arc geometry showing its most disorder tolerance. Surface disorder is inevitable in a real experimental setting with vacancies being its primary source. It is therefore interesting to examine this effect in our proposed $InNbSe_2$ WSM.

In order to perform simulation of vacancies on the surface of $InNbSe_2$, we use a combination of DFT with a coherent potential approximation (CPA)[60], a self–consistent method that allows to extract disorder induced self–energies $\hat{\Sigma}_{CPA}(E)$ from the FP–LMTO calculation. Our recent implementation within FP–LMTO method is described in Ref. [59]. Figure 6(a,b) shows evolution of the one–electron Fermi states of the $InNbSe_2$ slab structure that are projected onto the Se terminated surface for two concentrations, x=0.05 and x=0.1, respectively, of substitutional vacancies that we impose at its topmost Se layer. For both concentrations, the Fermi arcs are still visible and increasing the disorder results in broadening the arcs especially in the regions always from the Weyl points. Since the arcs electrons are continuously connected to the bulk Weyl points, the area in the vicinity of the Weyl points is less affected by disorder. We can contrast this behavior with the regular surface states which we expect to be more susceptible to surface disorder. We do not impose any bulk disorder in this calculation, therefore the bulk states projected onto the surface BZ are unaffected by the surface vacancies.

The situation is more complicated for the Fermi arcs appeared at the In terminated (001) surface. Figure 6(c,d) shows their behavior for x=0.05 and x=0.1, respectively. We notice that the arcs that connect the Weyl points in Fig 5(d) slightly change their shape with disorder which possibly connected to the effect induced by the real part of the disorder self–energy $Re\Sigma_{CPA}(E = E_F)$. One state is seen in this simulation to get closer to the $\bar{K}$ point of the surface BZ while another state has its shape resembling a regular bulk Fermi state projected onto the surface BZ. Both states acquire much less broadening if we compare them with other surface states that broaden a lot and almost disappear when x=0.1. As these arcs show a lot less curvature than the arcs resolved at Se terminated surface, we therefore speculate that this is likely the effect of the disorder tolerance for the straight Fermi arcs that we proposed in our recent work [59].

VI. SUMMARY

In summary, by using first–principles calculations, we investigated topological properties of layered materials $InNbS_2$ and $InNbSe_2$. Our theoretical analysis showed that $InNbS_2$ is a nodal line semimetal even with the presence of SOC as long as the mirror symmetry is preserved. This significant feature is different from previously proposed materials which normally neglect the SOC. $InNbSe_2$ is proposed to be a Type II WSM with 12 Weyl nodes at the same energy level. We also studied the Fermi arc surface states and confirmed their robustness against the surface disorder effects. These two compounds are quasi–2D and easy to cleave, therefore can potentially serve as an interesting platform for further experimental studies of topological electronic states.

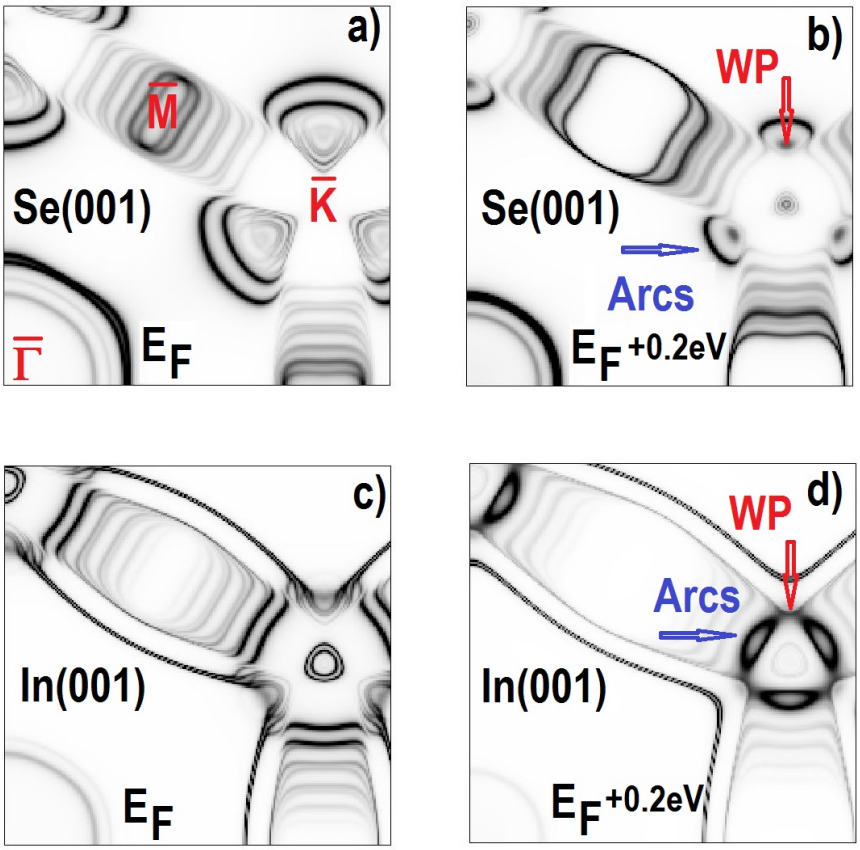

FIG. 5: (color online). Surface Fermi states of the $InNbSe_2$ slab for the Se terminated (a,b) and In terminated (c,d) (001) surfaces. The position of the Fermi level in (a) and (c) corresponds to the stoichiometric compound. Plots (b) and (d) show Fermi surfaces corresponding to the Fermi level shifted by 0.2 eV when it is tuned to the Weyl points to better visualize the appearance of the Fermi arcs.

ACKNOWLEDGEMENT

The work was supported by National Key R&D Program of China (No. 2017YFA0303203), the NSFC (No. 11525417, 11374147, 51572085, 51721001), National Key Project for Basic Research of China (Grant No. 2014CB921104), the Natural Science Foundation of Jiangsu Province (Grants No. BK20170821), the Priority Academic Program Development of Jiangsu Higher Education Institutions. S.S. was supported by NSF DMR (Grant No. 1411336).

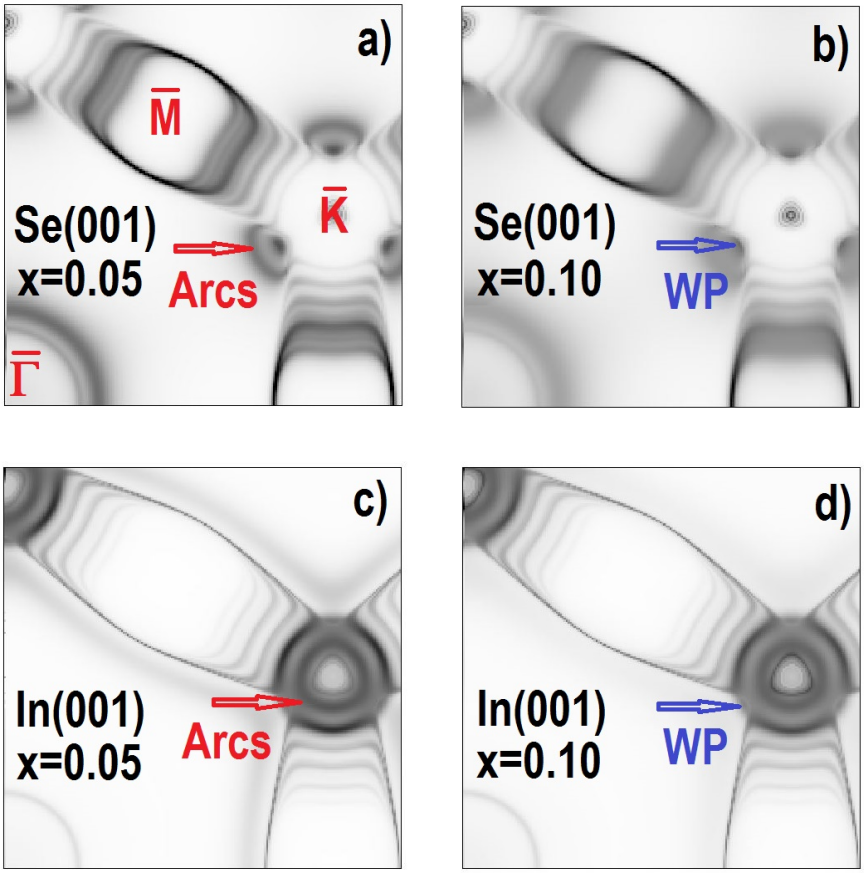

FIG. 6: (color online). Effect of surface vacancies on the surface Fermi states of the $InNbSe_2$ slab for the Se terminated (a,b) and In terminated (c,d) (001) surfaces. Plots (a) and (c) correspond to 5% of vacancies imposed at the top Se and bottom In layer, respectively. Plots (b) and (d) correspond to 10% of the vacancies. The Fermi level is tuned to the position of the Weyl points to better illustrate the degradation of the Fermi arc states.

* Electronic address: savrasov@physics.ucdavis.edu
† Electronic address: xgwan@nju.edu.cn

[1] X. Wan, A. M. Turner, A. Vishwanath, & S. Y. Savrasov, Topological semimetal and Fermi-arc surface states in the electronic structure of pyrochlore iridates. *Phys. Rev. B* **83**, 205101 (2011).
[2] L. Balents, Viewpoint: Weyl electrons kiss. *Physics* **4**, 36 (2011).
[3] S. M. Young, S. Zaheer, J. C. Y. Teo, C. L. Kane, E. J. Mele, & A. M. Rappe. Dirac Semimetal in Three Dimensions. *Phys. Rev. Lett.* **108**, 140405 (2012).
[4] B.-J. Yang, & N. Nagaosa, Classification of stable three-dimensional Dirac semimetals with nontrivial topology. *Nature Commun.* **5**, 4898 (2014). Z. Gao, M. Hua, H. Zhang & X. Zhang, Classification of stable Dirac and Weyl semimetals with reflection and rotational symmetry. *Phys. Rev. B* **93**, 205109 (2016).
[5] X.-L. Sheng, Z. Wang, R. Yu, H. Weng, Z. Fang, & X. Dai, Topological insulator to Dirac semimetal transition driven by sign change of spin-orbit coupling in thallium nitride. *Phys. Rev. B* **90**, 245308 (2014)
[6] Z. Wang, Y. Sun, X.-Q. Chen, C. Franchini, G. Xu, H. Weng, X. Dai, & Z. Fang. Dirac semimetal and topological phase transitions in A_3Bi (A = Na, K, Rb). *Phys. Rev. B* **85**, 195320 (2012).
[7] Z. Wang, H. M. Weng, Q. Wu, X. Dai, & Z. Fang, Three-dimensional Dirac semimetal and quantum transport in Cd_3As_2. *Phys. Rev. B* **88**, 125427 (2013).
[8] Q. D. Gibson, L. M. Schoop, L. Muechler, L. S. Xie, M. Hirschberger, N. P. Ong, R. Car, & R. J. Cava. Three-dimensional Dirac semimetals: Design principles and predictions of new materials. *Phys. Rev. B* **91**, 205128 (2015).
[9] Y. Du, B. Wan, D. Wang, L. Sheng, C.-G. Duan & X. Wan. Dirac and Weyl Semimetal in XYBi(X = Ba, Eu; Y = Cu, Ag and Au). *Sci. Rep.* **5**, 14423 (2015).
[10] A. A. Burkov, M. D. Hook, & L. Balents, Topological nodal semimetals. *Phys. Rev. B* **84**, 235126 (2011).
[11] H. Weng, Y. Liang, Q. Xu, R. Yu, Z. Fang, X. Dai, & Y. Kawazoe. Topological node-line semimetal in three-dimensional graphene networks. *Phys. Rev. B* **92**, 045108 (2015).
[12] R. Yu, H. Weng, Z. Fang, X. Dai, & X. Hu, Topological Node-Line Semimetal and Dirac Semimetal State in Antiperovskite Cu_3PdN. *Phys. Rev. Lett.* **115**, 036807 (2015)
[13] Y. Kim, B. J. Wieder, C. L. Kane & A. M. Rappe, Dirac Line Nodes in Inversion-Symmetric Crystals. *Phys. Rev. Lett.* **115**, 036806 (2015).
[14] X. Wan, A. Vishwanath, & S. Y. Savrasov, Computational Design of Axion Insulators Based on 5*d* Spinel Compounds. *Phys. Rev. Lett.* **108**, 146601 (2012).
[15] V. Aji, Adler-Bell-Jackiw anomaly in Weyl semimetals: Application to pyrochlore iridates. *Phys. Rev. B* **85**, 241101 (2012).
[16] D. T. Son, & B. Z. Spivak, Chiral anomaly and classical negative magnetoresistance of Weyl metals. *Phys. Rev. B* **88**, 104412 (2013).
[17] K.-Y. Yang, Y.-M. Lu, & Y. Ran, Quantum Hall effects in a Weyl semimetal: Possible application in pyrochlore iridates. *Phys. Rev. B* **84**, 075129 (2011).
[18] S. A. Parameswaran, T. Grover, D. A. Abanin, D. A. Pesin & A. Vishwanath, Probing the Chiral Anomaly with Nonlocal Transport in Three-Dimensional Topological Semimetals. *Phys. Rev. X* **4**, 031035 (2014).
[19] A. C. Potter, I. Kimchi & A. Vishwanath, Quantum oscillations from surface Fermi arcs in Weyl and Dirac semimetals. *Nature Commun.* **5**, 6161 (2014).
[20] A. A. Soluyanov, D. Gresch, Z. Wang, Q. Wu, M. Troyer, X. Dai & B. A. Bernevig. Type-II Weyl semimetals. *Nature* **527**, 495 (2015).
[21] T. E. O'Brien, M. Diez, & C. W. J. Beenakker, Magnetic Breakdown and Klein Tunneling in a Type-II Weyl Semimetal. *Phys. Rev. Lett.* **116**, 236401 (2016).
[22] G. Xu, H. M. Weng, Z. Wang, X. Dai & Z. Fang, Chern Semimetal and the Quantized Anomalous Hall Effect in $HgCr_2Se_4$. *Phys. Rev. Lett.* **107**, 186806 (2011).
[23] H. Weng, C. Fang, Z. Fang, B. A. Bernevig & X. Dai, Weyl semimetal phase in noncentrosymmetric transition-metal monophosphides. *Phys. Rev. X* **5**, 011029 (2015).
[24] S.-M. Huang, S.-Y. Xu, I. Belopolski, C.-C. Lee, G. Chang, B. Wang, N. Alidoust, G. Bian, M. Neupane, C. Zhang, S. Jia, A. Bansil, H. Lin & M. Z. Hasan. A Weyl Fermion semimetal with surface Fermi arcs in the transition metal monopnictide TaAs class. *Nat. Commun.* **6**, 7373 (2015).
[25] C. Shekhar, A. K. Nayak, Y. Sun, M. Schmidt, M. Nicklas, I. Leermakers, U. Zeitler, Y. Skourski, J. Wosnitza, Z. Liu, Y. Chen, W. Schnelle, H. Borrmann, Y. Grin, C. Felser & B. Yan. Extremely large magnetoresistance and ultrahigh mobility in the topological Weyl semimetal candidate NbP. *Nat. Phys.* **11**, 645 (2015).
[26] N. Xu, H. M. Weng, B. Q. Lv, C. E. Matt, J. Park, F. Bisti, V. N. Strocov, D. Gawryluk, E. Pomjakushina, K. Conder, N. C. Plumb, M. Radovic, G. Autès, O. V. Yazyev, Z. Fang, X. Dai, T. Qian, J. Mesot, H. Ding & M. Shi. Observation of Weyl nodes and Fermi arcs in tantalum phosphide. *Nat. Commun.* **7**, 11006 (2016).
[27] S. Xu, N. Alidoust, I. Belopolski, Z. Yuan, G. Bian, T.-R. Chang, H. Zheng, V. N. Strocov, D. S. Sanchez, G. Chang, C. Zhang, D. Mou, Y. Wu, L. Huang, C.-C. Lee, S.-M. Huang, B. Wang, A. Bansil, H.-T. Jeng, T. Neupert, A. Kaminski, H. Lin, S. Jia & M. Z. Hasan. Discovery of a Weyl fermion state with Fermi arcs in niobium arsenide. *Nat. Phys.* **11**, 748–754 (2015).
[28] L. Huang, T. M. McCormick, M. Ochi, Z. Zhao, M.-T. Suzuki, R. Arita, Y. Wu, D. Mou, H. Cao, J. Yan, N. Trivedi & A. Kaminski. Spectroscopic evidence for a type II Weyl semimetallic state in $MoTe_2$. *Nat. Materials* **15**, 1155-1160 (2016).
[29] G. Autès, D. Gresch, M. Troyer, A. A. Soluyanov & O. V. Yazyev, Robust Type-II Weyl Semimetal Phase in Transition Metal Diphosphides XP_2 (X =Mo, W). *Phys. Rev. Lett.* **117**, 066402 (2016).
[30] S.-Y. Xu, N. Alidoust, G. Chang, H. Lu, B. Singh, I. Belopolski, D. S. Sanchez, X. Zhang, G. Bian, H. Zheng, M.-A. Husanu, Y. Bian, S.-M. Huang, C.-H. Hsu, T.-R. Chang, H.-T. Jeng, A. Bansil, T. Neupert, Vl. N. Strocov, H. Lin, S. Jia and M. Z. Hasan. Discovery of Lorentz-violating type II Weyl fermions in LaAlGe. Sci. Adv. **3**, e1603266 (2017).
[31] B. Q. Lv, H. M. Weng, B. B. Fu, X. P. Wang, H. Miao, J. Ma, P. Richard, X. C. Huang, L. X. Zhao, G. F. Chen, Z. Fang, X. Dai, T. Qian, & H. Ding. Experimental discovery of Weyl semimetal TaAs. *Phys. Rev. X* **5**, 031013

(2015).

[32] B. Q. Lv, N. Xu, H. M. Weng, J. Z. Ma, P. Richard, X. C. Huang, L. X. Zhao, G. F. Chen, C. E. Matt, F. Bisti, V. N. Strocov, J. Mesot, Z. Fang, X. Dai, T. Qian, M. Shi & H. Ding. Observation of Weyl nodes in TaAs. *Nat. Phys.* **11**, 724–727 (2015).

[33] S.-Y. Xu, I. Belopolski, N. Alidoust, M. Neupane, G. Bian, C. Zhang, R. Sankar, G. Chang, Z. Yuan, C.-C. Lee, S.-M. Huang, H. Zheng, J. Ma, D. S. Sanchez, B. Wang, A. Bansil, F. Chou, P. P. Shibayev, H. Lin, S. Jia, M. Z. Hasan. Discovery of a Weyl fermion semimetal and topological Fermi arcs. *Science* **349**, 613–617 (2015).

[34] D.-F. Xu, Y. Du, Z. Wang, Y.-P. Li, X.-H. Niu, Q. Yao, P. Dudin, Z.-A. Xu, X. Wan, D.-L. Feng. Observation of Fermi Arcs in Non-Centrosymmetric Weyl Semi-Metal Candidate NbP. *Chin. Phys. Lett.* **32**, 107101 (2015).

[35] C. Fang, Y. Chen, H.-Y. Kee & L. Fu, Topological nodal line semimetals with and without spin-orbital coupling. *Phys. Rev. B* **92**, 081201(2015).

[36] Xu, Q., Yu, R., Fang, Z., Dai, X. & Weng, H. Topological nodal line semimetals in the CaP_3. *Phys. Rev. B* **95**, 045136 (2017).

[37] Huang, H., Liu, J., Vanderbilt, D. & Duan, W. Topological nodal-line semimetals in alkaline-earth stannides, germanides, and silicides. *Phys. Rev. B* 93, 201114 (2016).

[38] Y. Du, F. Tang, D. Wang, L. Sheng, E.-j. Kan, C.-G. Duan, S. Y. Savrasov & X. Wan. CaTe: a new topological node-line and Dirac semimetal. *npj Quantum Materials* **2**, 3 (2017).

[39] Mullen, K., Uchoa, B. & Glatzhofer, D. T., Line of Dirac Nodes in Hyperhoneycomb Lattices. *Phys. Rev. Lett.* **115**, 026403 (2015).

[40] L. Xie, L. M. Schoop, E. M. Seibel, Q. D. Gibson, W. Xie, & R. J. Cava. A new form of Ca_3P_2 with a ring of Dirac nodes. *APL Materials* **3**, 083602 (2015).

[41] M. Zeng, C. Fang, G. Chang, Y.-A. Chen, T. Hsieh, A. Bansil, H. Lin, L. Fu. Topological semimetals and topological insulators in rare earth monopnictides. Preprint at https://arxiv.org/abs/1504.03492 (2015).

[42] Y.-H. Chan, C.-K. Chiu, M. Y. Chou & A. P. Schnyder, Ca_3P_2 and other topological semimetals with line nodes and drumhead surface states. *Phys. Rev. B* **93**, 205132 (2016).

[43] G. Bian, T.-R. Chang, H. Zheng, S. Velury, S.-Y. Xu, T. Neupert, C.-K. Chiu, S.-M. Huang, D. S. Sanchez, I. Belopolski, N. Alidoust, P.-J. Chen, G. Chang, A. Bansil, H.-T. Jeng, H. Lin, and M. Z. Hasan. Drumhead surface states and topological nodal-line fermions in $TlTaSe_2$. *Phy. Rev. B* **93**, 121113(R) (2016).

[44] G. Bian, T.-R. Chang, R. Sankar, S.-Y. Xu, H. Zheng, T. Neupert, C.-K. Chiu, S.-M. Huang, G. Chang, I. Belopolski, D. S. Sanchez, M. Neupane, N. Alidoust, C. Liu, B. Wang, C.-C. Lee, H.-T. Jeng, C. Zhang, Z. Yuan, S. Jia, A. Bansil, F. Chou, H. Lin & M. Z. Hasan., Topological nodal-line fermions in spin-orbit metal $PbTaSe_2$. *Nature Communs.* **7**, 10556 (2015).

[45] T. T. Heikkila & G. E. Volovik, Flat bands as a route to high-temperature superconductivity in graphite. Preprint at https://arxiv.org/abs/1504.05824 (2015).

[46] N. B. Kopnin, T. T. Heikkila & G. E. Volovik, High-temperature surface superconductivity in topological flat-band systems. *Phys. Rev. B* **83**, 220503 (2011).

[47] J. P. Perdew, K. Burke & M. Ernzerhof, Generalized Gradient Approximation Made Simple. *Phys. Rev. Lett.* **77**, 3865 (1996).

[48] N. Karnezos, L. B. Welsh & M. W. Shafer, Structural and NMR properties of niobium dichalcogenides intercalated with post transition metals. *Phy. Rev. B* **11**, 1808-1917 (1975).

[49] C. S. Sunandana, K. Chandrasekaran, G. Aravamudan & G. V. Subbarao, Electrical properties of $InxMCh_2$ (M≡Nb, Ta; Ch≡S, Se) *J. Less-Common Metals*, **84**, 115 (1982).

[50] E. A. Marseglia, Transition Metal Dichalcogenides and Their Intercalates. *Int. Rev. Phys. Chem.* **3**, 177 (1983).

[51] S. Grimme, J. Antony, S. Ehrlich, and S. Krieg, "A consistent and accurate ab initio parametrization of density functional dispersion correction (dft-d) for the 94 elements H-Pu", J. Chem. Phys. **132**, 154104 (2010). S. Grimme, S. Ehrlich, and L. Goerigk, "Effect of the damping function in dispersion corrected density functional theory", J. Comp. Chem. **32**, 1456 (2011).

[52] The experimental lattice parameter for $InNbS_2$: a=b=3.34Å and c=8.16Å. The coordinate of S is (1/3, 2/3, 0.32). The experimental lattice constant for $InNbSe_2$: a=b=3.45Å and c=9.27Å. The coordinate of Se is (0, 0 ,0.31). The theoritical lattice constant for $InNbS_2$: a=b=3.346Å and c=8.11Å. The relaxed coordinate of S is (1/3, 2/3, 0.306). Th theoritical lattice constant for $InNbSe_2$: a=b=3.41Å and c=9.18Å. The relaxed coordinate of Se is (0, 0, 0.316).

[53] S. Y. Savrasov, Linear-response theory and lattice dynamics: a muffin-tin-orbital approach, *Phys. Rev. B* **54**, 16470 (1996).

[54] P. Blaha, K. Schwarz, G. K. H. Madsen, D. Kvasnicka & J. Luitz, WIEN2K, An Augmented Plane Wave+ Local Orbitals Program for Calculating Crystal Properties (Karlheinz Schwarz, Technische Universitat Wien, Austria, 2001).

[55] F. Tran & P. Blaha, Accurate Band Gaps of Semiconductors and Insulators with a Semilocal Exchange-Correlation Potential. *Phys. Rev. Lett.* **102**, 226401 (2009).

[56] T. Fukui, Y. Hatsugai & H. Suzuki, Chern Numbers in Discretized Brillouin Zone: Efficient Method of Computing (Spin) Hall Conductances. *J. Phys. Soc. Jpn.*, **74**, 6 (2005).

[57] M. Taillefumier, V. K. Dugaev, B. Canals, C. Lacroix & P. Bruno, Chiral two-dimensional electron gas in a periodic magnetic field: Persistent current and quantized anomalous Hall effect. *Phys. Rev. B* **78**, 155330 (2008).

[58] In fact, both the LMTO and LAPW methods assume improved projectors that include both the radial wave functions and their energy derivatives in order to better describe orbital partial characters of the one–electron states. See, O. K. Andersen, Linear methods in band theory. *Phys. Rev. B* **12**, 3050 (1975).

[59] G. Resta, S.-T. Pi, X. Wan & S. Y. Savrasov, High Surface Conductivity of Fermi Arc Electrons in Weyl semimetals. Preprint at https://arxiv.org/abs/1708.02415 (2017).

[60] For a review, see, e.g., F. Yonezawa & K. Morigaki, Coherent potential approximation: basic concepts and applications. *Prog. Theo. Phys. Supp.* **53**, 1–76 (1973).